CFD and Experimental Validation of a Gas-Based Thermocline TES System for CSP Applications with Nanofluid Modeling Perspective

CFD and Experimental Validation of a Gas-Based Thermocline TES System for CSP Applications with Nanofluid Modeling Perspective

Mohamed Shameer Peer[1], Giorgio Cau[1], Mario Cascetta[1], Tsega Y. Melesse[1], Mattia Braggio[1], and Mario Petrollese[1*]

[1] Department of Mechanical, Chemical and Materials Engineering, University of Cagliari, Cagliari, Italy

[*]E-mail: mario.petrollese@unica.it

Abstract. This paper presents an integrated experimental and numerical study of a thermocline-based packed-bed thermal energy storage (TES) system employing nitrogen as the heat transfer fluid (HTF), designed for use in Concentrated Solar Power (CSP) applications. A full-scale laboratory setup was developed at the University of Cagliari to investigate charging behavior under various nitrogen flow rates. Axial temperature evolution was measured using an array of 16 thermocouples and compared against predictions from a three-dimensional CFD model developed in ANSYS Fluent. The CFD model incorporates a porous media approach with Ergun-based resistance parameters and was validated against experimental temperature profiles and pressure drop data. Detailed plots of temperature and velocity distributions confirm strong thermal stratification and accurate thermocline formation. The model captures the progression of the thermal front across the packed bed and agrees closely with experimental sensor data, confirming the accuracy of the simulated heat transfer dynamics. In parallel, a mathematical model was formulated to evaluate nanofluid inclusion, using CuO–nitrogen mixtures at low volume fractions. The model predicts enhanced thermal conductivity and energy storage potential. Based on mathematical modeling, the inclusion of CuO nanoparticles in nitrogen is projected to increase thermal conductivity and convective heat transfer coefficient, while reducing pressure drop. These predicted enhancements indicate the potential for sharper thermocline formation, improved energy storage efficiency, and reduced hydraulic losses; paving the way for more compact and effective TES systems in solar thermal applications.

Keywords. *Thermal Energy Storage, Thermocline, Packed Bed, CFD Simulation, Nanofluid, CSP*

1. Introduction

The transition to renewable energy sources is accelerating globally, with Concentrated Solar Power (CSP) emerging as a promising solution for dispatchable and scalable solar electricity generation. CSP is a sustainable technology that produces electrical energy with no carbon

dioxide emissions, making it suitable for a wide range of industrial applications [1]. However, the intermittent nature of solar irradiation, particularly during transient weather conditions and nighttime hours, limits the continuous operation of CSP plants. This challenge underscores the importance of integrating thermal energy storage (TES) systems to buffer solar energy and decouple generation from consumption.

Among the various TES architectures, thermocline-based packed-bed systems have gained significant attention due to their simplicity, cost-effectiveness, and high energy density. These systems utilize a single tank filled with solid media, where a temperature gradient or "thermocline" forms between the hot and cold zones during charging and discharging. As demonstrated by Cascetta et al. [2], thermocline designs can offer up to 45% cost savings compared to conventional systems, without significant performance compromise.

To date, most TES systems in CSP plants have employed liquid-phase heat transfer fluids (HTFs) such as molten salts or thermal oils. Molten salts and thermal oils have high freezing points, are corrosive to system components, and require complex system management to prevent solidification and corrosion [3,4]. In contrast, gaseous HTFs, such as like nitrogen and helium are non-reactive, reducing corrosion and material issues in system components [5]. However, gas-based TES systems have lower energy density compared to those using liquids or solids, making them less suitable for applications where space is limited or high storage capacity is needed [6]. Achieving high round-trip efficiency is more difficult, as more energy is lost during charging and discharging cycles [7]. These factors limit CSP's standalone efficiency in packed-bed TES applications.

To address these limitations, nanofluid technologies, which involve dispersing nanoparticles into a base fluid to enhance thermal properties, have emerged as a promising solution [8,9]. As reported by Lougou et al, adding CuO nanoparticles to molten salts or heat transfer fluids significantly increases their thermal conductivity (by up to 39.55%) and thermal diffusivity (by up to 37.23%), allowing for faster and more efficient heat transfer in CSP systems [10]. Moreover, Aljaerani et al. demonstrated CuO nanoparticles can boost the specific heat capacity (up to 10.51% in chloride salts and 5.6% in nitrate salts) and latent heat (up to 30%), improving the material's ability to store thermal energy [11]. The optimal enhancement is often achieved at low concentrations (e.g., 0.1–0.7% by mass), balancing improved thermal properties with manageable viscosity and stability [12]. CuO nanoparticles can significantly enhance the thermal properties of heat transfer and storage materials in CSP systems, leading to improved efficiency and energy storage. Optimal results depend on nanoparticle concentration, dispersion, and fluid compatibility. This approach is a promising avenue for advancing CSP technology.

Despite these advancements, critical gaps remain in the development of high-temperature, gas-phase thermocline systems for CSP applications. Specifically:

- Validated experimental–numerical studies using gaseous HTFs are limited.
- Full-scale CFD models are rarely benchmarked against dense thermocouple-based measurements.
- Nanoparticle-enhanced gas HTFs remain largely theoretical, with no unified framework connecting base-case validation to nanoparticle performance projections.

This study addresses these gaps through an integrated experimental and computational approach to evaluate a nitrogen-based thermocline TES system developed at at the "TES Technologies" lab of the University of Cagliari. A packed-bed storage tank filled with alumina spheres was tested under controlled high-temperature nitrogen charging conditions. Axial temperature distributions were measured with a dense thermocouple array to characterize

thermocline formation and thermal front propagation. A detailed three-dimensional CFD model was developed in ANSYS Fluent and validated against experimental data. The model incorporates porous media physics, realistic inlet conditions, and temperature-dependent thermophysical properties of both the nitrogen gas and alumina packing material. The simulation accurately reproduces thermocline behavior, pressure drop, and thermal stratification observed in the experiments. In addition, the paper introduces a mathematical model for nanofluid enhancement using CuO–nitrogen suspensions. The model predicts improved thermal conductivity and potential reductions in thermocline thickness, laying the foundation for future nanofluid-based CFD studies and experimental trials.

2. Experimental Setup

The experimental investigation was conducted at the University of Cagliari using a laboratory-scale packed-bed TES system as shown in Figure 1. The objective was to evaluate the thermal stratification and charging behavior of a thermocline TES unit using nitrogen gas as the HTF under high-temperature operating conditions relevant to CSP applications.

Figure 1. Test rig with thermal energy storage system.

The TES system consists of a vertically oriented cylindrical tank fabricated from stainless steel, with an internal height of 1.2 m and diameter of 0.3 m, however the active packed-bed region is limited to 0.9 m in height. The tank is filled with spherical alumina balls of 2 mm diameter, selected for their high thermal conductivity, thermal shock resistance, and chemical stability. Figure 2 represents the cylinder filled with alumina balls.

Figure 2. Cylindrical tank filled with alumina balls

The tank is externally insulated with ceramic fiber blankets (thickness 100 mm, thermal conductivity ~0.035 W/m·K) to minimize radial heat losses. Internally, perforated stainless-steel mesh filters support the particle bed and ensure uniform gas distribution. Upper and lower plenum chambers are integrated to facilitate even inlet and outlet flow conditions. Nitrogen gas is supplied from high-pressure industrial cylinders via a regulated valve and delivered through a mass flow controller (±2% full scale accuracy). The gas is preheated using a 4.5 kW electrical cartridge heater, capable of reaching inlet temperatures of up to 500 °C.

The experimental campaigns focused on charging cycles, where preheated nitrogen was injected at different flow rates ranging from 10 to 30 Nm^3/h. The tank operated at slightly above atmospheric pressure (~1.2 bar). Ambient temperature conditions at the start of each run were approximately 25 °C, and full thermal relaxation was ensured between tests.

To capture the axial temperature distribution, nineteen K-type thermocouples (Ø1.5 mm, class 1, accuracy ±1.5 °C) were embedded along the central vertical axis of the packed bed as shown in Figure 3. Only the top 16 thermocouples were considered for the experimental validation of the CFD model, as alumina beads were filled up to the height corresponding to T16. The remaining three thermocouples (T17–T19) were positioned below the supporting frame and did not reflect the thermal behavior of the packed-bed region.

A pressure transducer (0–2 bar range, accuracy ±0.5% FS) was mounted at mid-height to monitor dynamic pressure fluctuations. All sensors were connected to a National Instruments cDAQ system and sampled at 1 Hz using a custom LabVIEW interface for real-time data visualization and logging.

Thermocouples	Positioning [mm]
T01	894
T02	842
T03	794
T04	743
T05	695
T06	648
T07	597
T08	547
T09	499
T10	452
T11	399
T12	346
T13	294
T14	250
T15	192
T16	145
T17	95
T18	45
T19	0

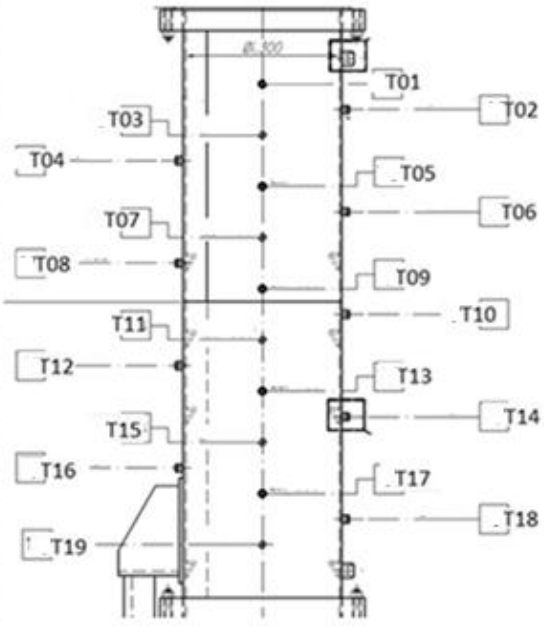

Figure 3. Position of thermocouples inside the tank

3. CFD Modeling

A three-dimensional CFD model of the TES system was developed using ANSYS Fluent to simulate the thermal and flow behavior of nitrogen during the charging process. The model replicates the

experimental configuration and is validated using temperature measurements and observed pressure drops across the packed bed.

The TES column geometry was recreated with full-scale dimensions: a 0.9 m high cylindrical packed bed (0.3 m diameter), upper and lower plenums, and inlet/outlet manifolds. The packed bed region was treated as a homogeneous porous domain, while the upper and lower plenums were modeled as free-flow zones. A structured hexahedral mesh was generated, with grid refinement near the inlet, thermocouple locations, and wall boundaries to improve solution accuracy, particularly for capturing steep thermal and velocity gradients.

A mesh independence study was performed across three grid densities. The final mesh of ~580,000 cells provided <3.5% deviation in outlet temperature and stable simulation time. Table 1 represents the boundary and initial conditions considered. A fixed time-step of 3 seconds was used throughout the transient CFD simulation, aligned with the experimental data acquisition interval. A total simulation time of 4500 seconds was covered, corresponding to 1500 iterations.

Table 1. Boundary and Initial Conditions.

Boundary	Specification
Inlet	Mass flow inlet (27g/s), 140°C
Wall	Convection (ceramic insulation)

3.1 Assessment of the pressure drop

Ergun's equation, which is commonly used to predict pressure drop across a wide range of velocities and is validated by experimental and simulation data [13,14], was included in the modelling as follows:

$$\frac{|\Delta p|}{L} = C_1 \cdot u + C_2 \cdot u^2 \quad (1)$$

$$C_1 = \frac{150}{d_p^2}\mu_f\frac{(1-\varepsilon)^2}{\varepsilon^3}\ (Viscous\ coefficient) \quad (2)$$

$$C_2 = \frac{1.75}{d_p}\rho_f\frac{(1-\varepsilon)}{\varepsilon^3}\ (Inertial\ coefficient) \quad (3)$$

where L is the porous medium length, u is the fluid speed, d_p is the particle diameter and ε represents the porosity of the bed. Using the obtained pressure drop data, the viscous and inertial resistance coefficients needed for Ergun's equation were calculated for the porous medium. These coefficients will be incorporated into the CFD model to accurately define the porous characteristics of the filter and supporting frame. The high viscous resistance coefficient suggests significant flow resistance, which is essential for efficient filtration, while the inertial coefficient contributes to the overall pressure loss due to flow acceleration effects [15].

3.2 Porous Zone Modelling

The TES column was discretized into multiple subregions based on their structural and functional roles as shown in Figure 4. Specifically, the porous domains were categorized into (i) the packed bed filled with alumina balls, (ii) the lower mesh support structure, and (iii) the inlet/outlet filters. Each of these domains exhibits different porosity characteristics and flow resistance behavior and was individually characterized for CFD implementation.

The porosity coefficient for alumina bead was calculated using void fractions and solid volume ratios. Specifically, by considering the geometrical volume (0.05272 m^3), the mass of alumina balls charged into the tank (141.16 kg), a porosity of about 40% has been assumed. Additionally, the heat transfer from the nitrogen gas to the alumina beads was analyzed to ensure the thermal interaction was correctly captured in the CFD model.

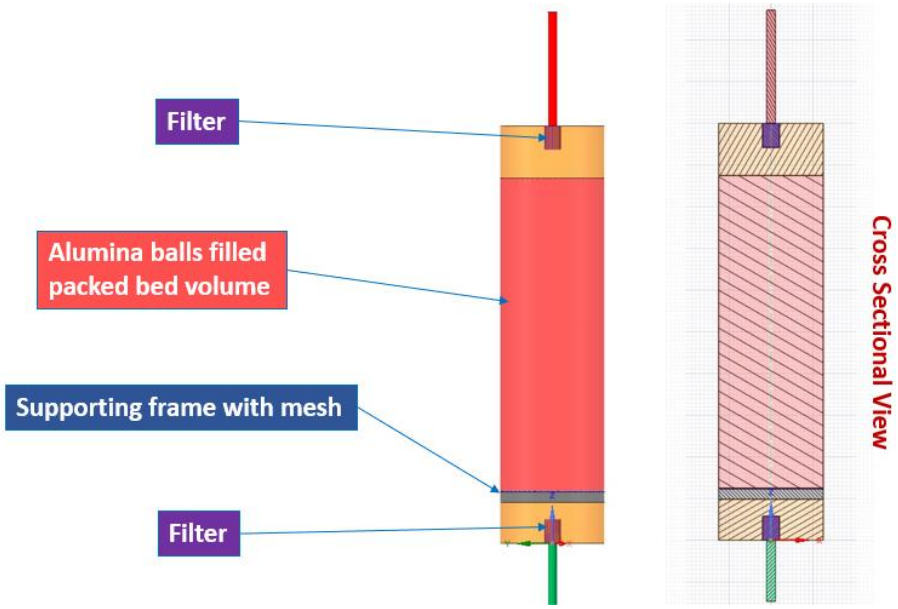

Figure 4. Representation of Porous media

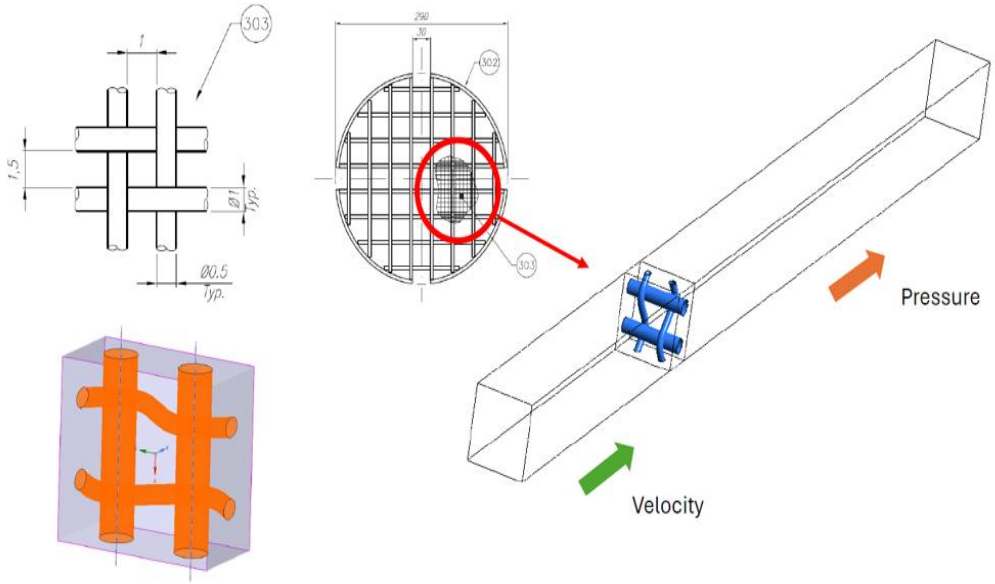

Figure 5. Cross Section view of grid sheet at supporting frame location

The metallic grid sheets used at the top and bottom of the packed bed act as filters and mechanical supports. Unlike the bulk bed, their resistance behavior was not estimated from geometry but derived from a dedicated CFD subdomain study. By simulating air flow through a unit cell of the mesh, the velocity–pressure drop relationship was obtained. Their flow resistance behavior was not calculated from geometry-based estimations but obtained through a dedicated CFD subdomain study. This involved simulating steady-state flow through a representative unit

cell of the mesh to determine the pressure drop as a function of inlet velocity. Figure 5 shows the considered isolated grid based structure implemented to examine pressure drop and velocity profiles.

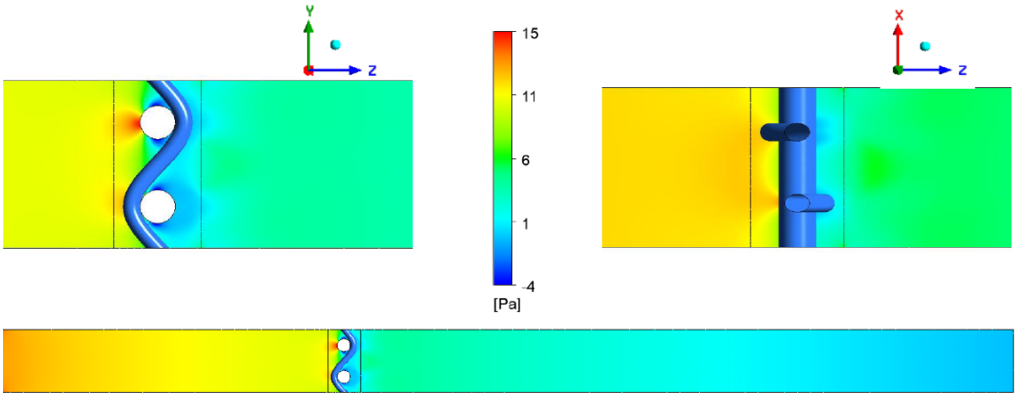

Figure 6. Pressure Contour of Grid sheet

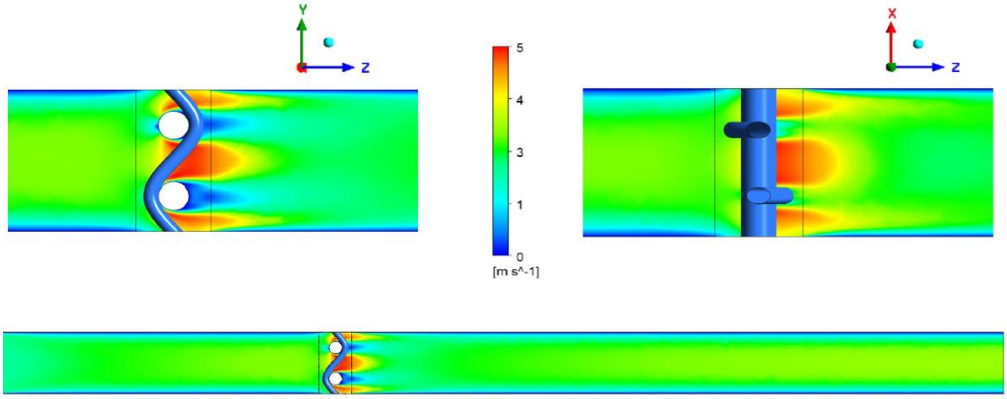

Figure 7. Pressure Contour of Grid sheet

CFD analyses reveal pressure contour variations (Figure 6) across the grid sheet, highlighting differences in flow resistance due to porous structures. Velocity contour maps (Figure 7) illustrate changes in flow velocity. As mentioned, the CFD simulation was conducted to analyze the pressure drop characteristics of a porous medium, specifically a grid sheet, under varying velocity conditions. The study aimed to determine the porous coefficients essential for modeling filtration and structural support in engineering applications.

The results, as shown in Figure 8, indicate the pressure drop (Δp) across the porous medium for different flow velocities. The pressure drop increases significantly with velocity, confirming the resistance offered by the medium to fluid flow. The values of Δp at higher velocities indicate a considerable pressure drop, possibly due to enhanced turbulence and flow separation effects in the porous region. High velocities induce turbulence and local flow separation within the pores, leading to energy losses and a sharp increase in pressure drop [16]. The size, shape, and connectivity of pores, as well as the overall porosity, strongly influence how pressure drop scales with velocity. Smaller pores and more complex geometries generally result in higher pressure drops at the same velocity [17]. Figure 8 represents the grid performance.

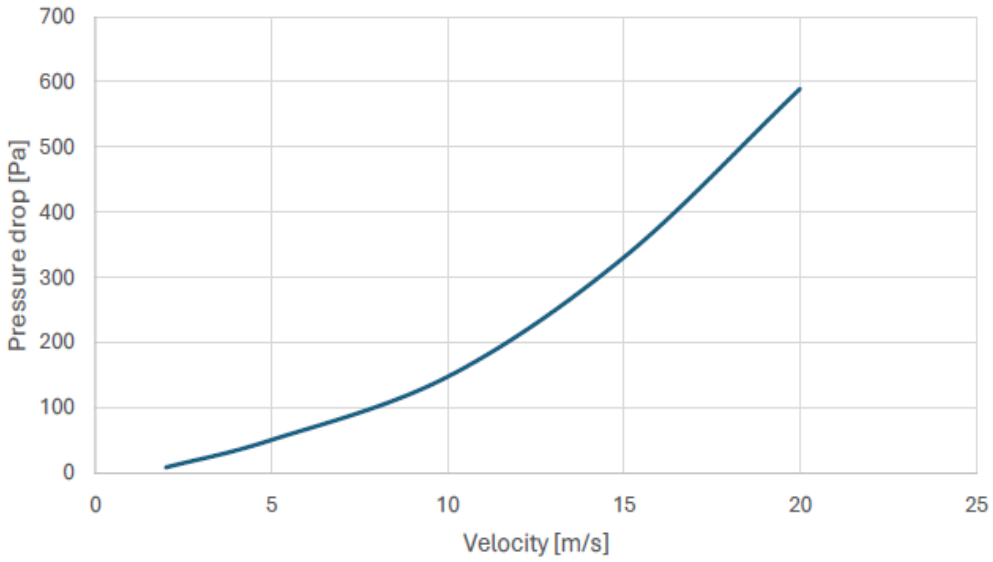

Figure 8. Grid performance curve – velocity/pressure drop relationship

The pressure drop versus velocity curve obtained from the grid sheet simulations (Figure 8) was used to extract the best-fit values of the porous coefficients: a viscous resistance coefficient of $4.52\times10^{7}\ m^{-2}$ and an inertial resistance coefficient of $1.53\times10^{3}\ m^{-1}$. These coefficients were then applied to both the filter zone and the support mesh in Fluent as porous domains with user-defined momentum sink terms. A porosity of 0.25 was assigned to the filter and support mesh zones, based on the grid sheet geometry (1 mm × 1.5 mm wire with 1 mm gap).

As the same grid sheet is used for both filters and mesh over supporting frames, the extracted porous coefficients will be used to model the two filters and supporting frame, ensuring accurate simulation of flow resistance and pressure drop in the system.

4. Results and Discussion: CFD–Experimental Validation

4.1 Temperature and Velocity Plots

Figures 9 and 10 present detailed CFD visualizations of temperature and velocity distributions within the packed-bed TES system during the nitrogen charging phase. The temperature contours (Figure 9) shows that a clear temperature gradient develops, separating warmer upper layers from cooler lower layers, resulting in effective thermal stratification and minimal mixing between layers [18]. The streamline view confirms smooth downward flow with minimal disturbances, while the cross-sectional (CS) view highlights uniform temperature layering. Cross-sectional views often reveal well-defined, uniform temperature layers, confirming the presence of stratification [19].

The velocity magnitude plots (Figure 10) reveal the behavior of flow as it enters, passes through, and exits the porous medium. Uniform flow distribution, effective damping by the packed bed, and limited recirculation near the top and bottom regions confirm that the system geometry supports stable thermal and fluid dynamic performance throughout the operation.

A rigorous comparison between CFD predictions and experimental data was performed to validate the accuracy of the simulation model. The validation encompasses thermal behavior across the TES column and the pressure drop induced by the porous bed. Figure 11 presents the time-dependent temperature rise recorded at various thermocouple locations distributed along

the vertical axis of the TES column, compared against the CFD simulation. Each dashed line represents the experimental profile at a fixed axial height, while the corresponding solid line shows the CFD result.

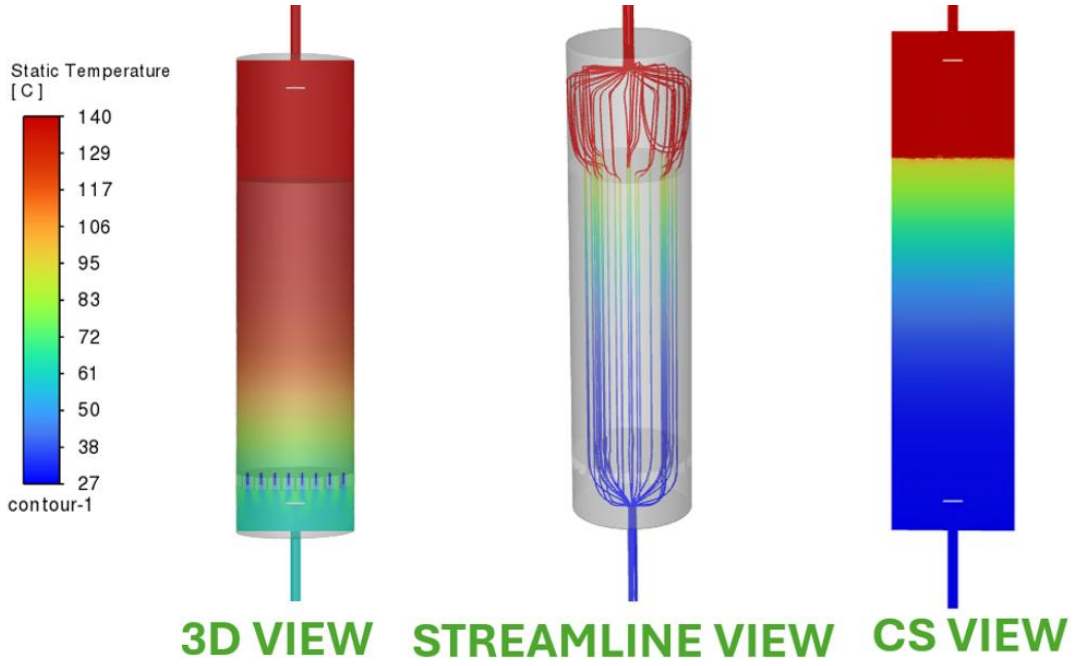

Figure 9. Temperature plots of Thermocline bed

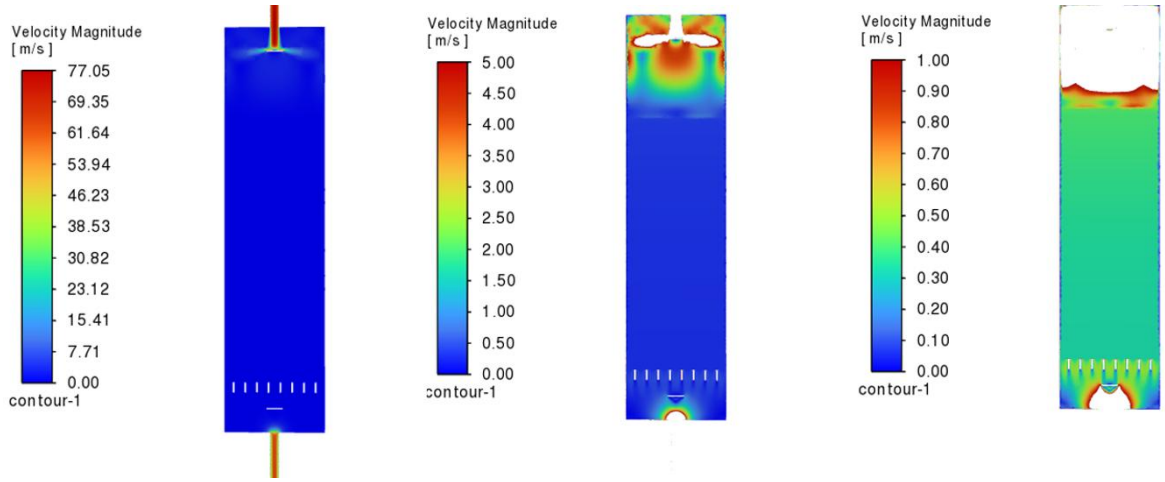

Figure 10. Velocity plots of Thermocline bed (Cross -Section Views)

The figure demonstrates smooth, downward propagation of the thermal front from the inlet (top) to the outlet (bottom), characteristic of well-formed thermocline behavior. Alumina beads maintain a relatively sharp thermocline, especially compared to some other materials [20]. The spacing and gradient of these curves illustrate the degree of thermal stratification established during the charging cycle. The simulation accurately captures both the timing and shape of the temperature rise at most locations. Small deviations are seen near the lower sensors, with a maximum absolute error of 4.2 °C, while the overall mean error remains around 2.8 °C. The relative error across the full dataset is below 3%, confirming that the model resolves heat exchange effectively.

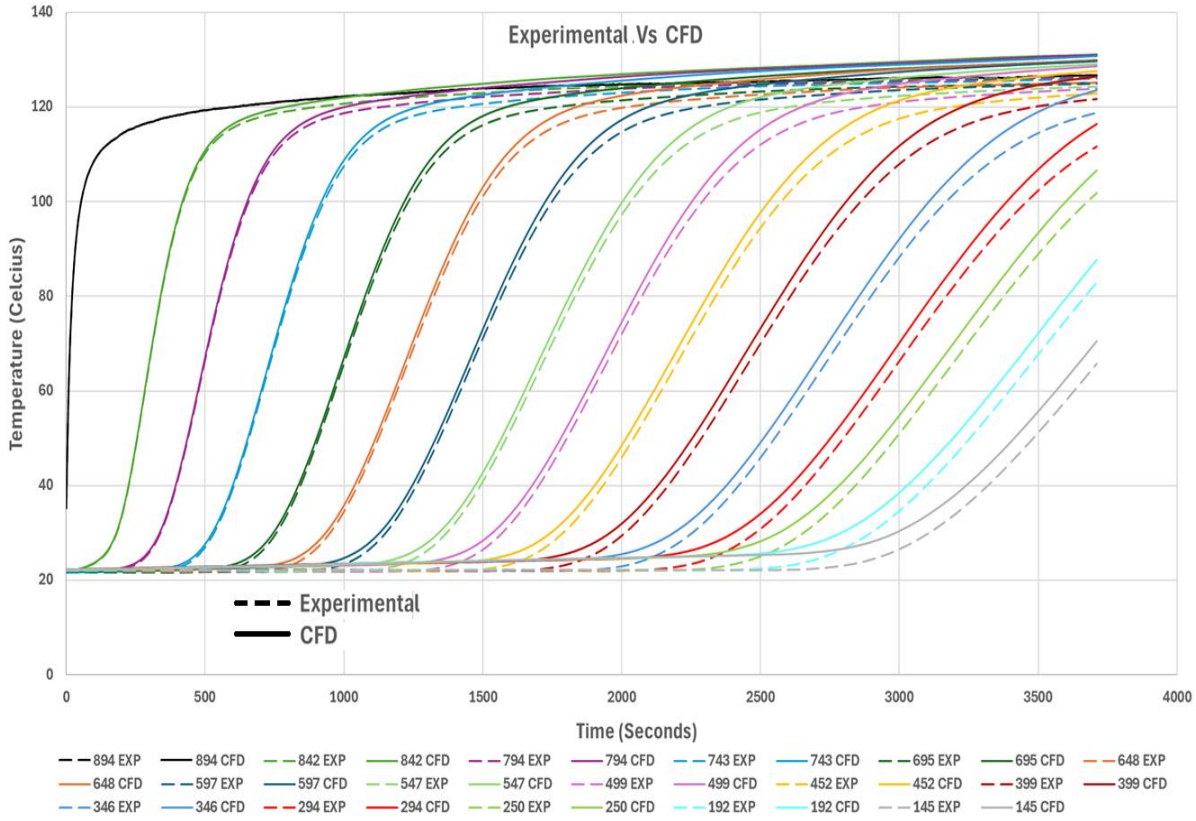

Figure 11. Experimental vs. CFD temperature evolution at each thermocouple location during charging

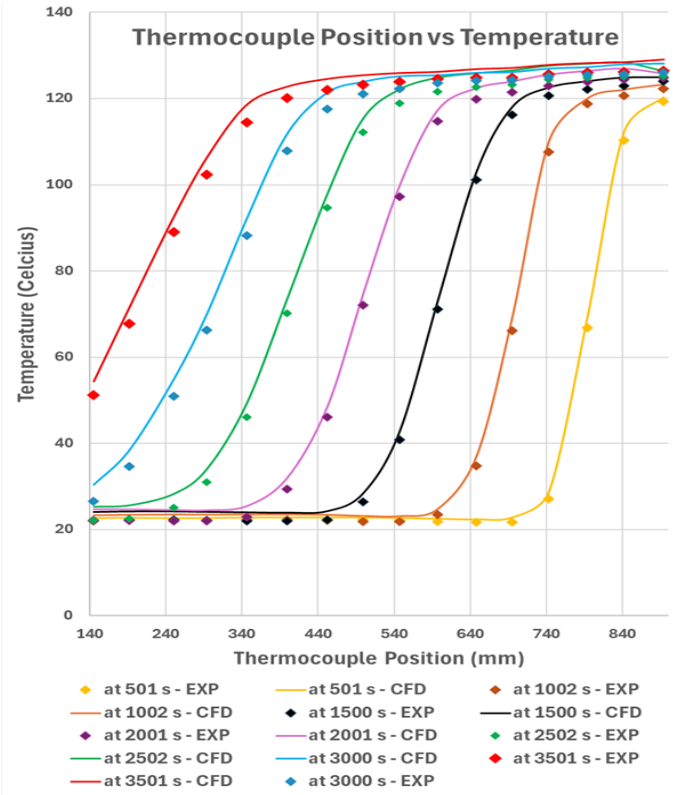

Figure 12. Axial temperature distribution at selected time intervals: comparison of experimental and CFD

Figure 12 shows axial temperature profiles plotted at six different time instants during the charging cycle. Each profile connects all thermocouples along the TES height, giving an instantaneous snapshot of the thermal distribution within the packed bed.

The experimental profiles show sharp thermal gradients that progressively shift downward as time advances, demonstrating the evolution of the thermocline region. The CFD predictions mirror this behavior well, with strong agreement in both the temperature plateau regions and the transition zones. The steepness of the gradient confirms limited thermal mixing, validating the laminar flow regime and the bed's ability to suppress turbulent diffusion [21].

This stratification quality directly influences the energy storage effectiveness. A sharp thermocline ensures that a larger volume of the bed remains at high temperature, maximizing extractable energy and reducing thermal degradation at discharge [22,23].

In addition to thermal validation, the CFD model was benchmarked against the measured pressure drop across the packed bed at a flow rate of 27 g/s. The experimental average pressure drop was 764.16 Pa, while the CFD simulation predicted 839 Pa, resulting in a relative error of approximately 9.7%. This agreement confirms the effectiveness of the Ergun-based porous media resistance formulation used in Fluent. The correct prediction of pressure losses is critical to estimate the pumping power required and to assess parasitic energy consumption in TES integration within CSP plants [24].

The validated CFD and experimental results together demonstrate that the packed-bed thermocline TES system provides efficient energy storage under nitrogen gas operation. The temperature evolution plots confirm that the system maintains a sharp thermocline throughout the charging cycle, with minimal axial mixing and strong thermal stratification; key characteristics for maximizing usable thermal capacity. The spatial profiles further validate that over time, the hot-cold interface propagates smoothly through the bed while maintaining a narrow transition region, ensuring that a large portion of the storage medium reaches and sustains high temperatures. This behavior directly contributes to a high energy storage density and thermal quality at discharge. Furthermore, the accurately predicted pressure drop ensures that the energy input required for gas circulation remains within acceptable limits, reducing losses.

5. Impact of Nanoparticles on Thermophysical Properties

To incorporate the thermo-fluid dynamic effects of CuO nanoparticles dispersed in nitrogen gas, a nanofluid model was developed using effective thermophysical property correlations derived from the literature. All property calculations were initially performed manually in a spreadsheet environment, without dedicated simulation software. This section presents the modeling framework, key assumptions, and resulting modifications in fluid properties that will serve as inputs for future CFD implementation. In the next phase, these formulations will be translated into MATLAB for parametric analysis and integrated into ANSYS Fluent simulations to evaluate the enhanced thermal performance of nanofluid-based TES systems. To calculate the main thermal properties of the nano the following correlations are used assuming the mixture as a homogenous media:

- Thermal Conductivity (k_{nf}) — Maxwell Model [25]:

$$\frac{k_{nf}}{k_{bf}} = \frac{k_{np}+2k_{bf}+2(k_{np}-k_{bf})\phi}{k_{np}+2k_{bf}-(k_{np}-k_{bf})\phi} \quad (4)$$

Where k_{bf} is the thermal conductivity of the base fluid (nitrogen), and ϕ is the nanoparticle volume fraction.

- Dynamic Viscosity (μ_{nf}) — Brinkman Model [26]:

$$\mu_{nf} = \frac{\mu_{bf}}{(1-\phi)^{2.5}} \quad 5)$$

Where μ_{bf} is the dynamic viscosity of the base fluid (nitrogen)

- Density (ρ_{nf}) [26]

$$\rho_{nf} = (1-\phi)\rho_{bf} + \phi\rho_{np} \quad 6)$$

Where ρ_{bf} and ρ_{np} are the density of the base fluid (nitrogen) and nanoparticles, respectively.

- Specific Heat ($C_{p,nf}$) [27]:

$$C_{p,nf} = \frac{\rho_{bf}C_{p,bf}(1-\phi)+\rho_{np}C_{p,np}\phi}{\rho_{nf}} \quad 7)$$

Where $C_{p,bf}$ and $C_{p,np}$ are the specific heat of the base fluid (nitrogen) and nanoparticles, respectively.

The incorporation of CuO nanoparticles into nitrogen gas at a volume fraction of ϕ = 0.05% leads to significant changes in thermophysical properties that collectively enhance the performance of the TES system as reported in Table 2.

Table 2. Derived Parameters at ϕ = 0.05%.

Property	Pure N_2	CuO–N_2 (ϕ =0.05%)	% Change
ρ (kg/m^3)	2.391	5.640	+135.9%
μ (Pa·s)	2.28 x10^{-5}	2.27 x10^{-5}	–0.35%
Cp (J/kg·K)	1040	738	–29.0%
k (W/m·K)	0.03297	0.03850	+16.8%
Re	33.57	33.68	~0.35%
Pr	0.718	0.435	–39.4%
h (W/m^2·K)	166.65	170.84	+2.5%
ΔP/L (kPa/m)	5.67	2.40	–57.7%

The mixture density increases by over 135%, primarily due to the high intrinsic density of CuO, contributing to greater thermal inertia [28]. Interestingly, the dynamic viscosity shows a slight decrease (–0.35%), indicating that at low concentrations, the nanoparticles remain well-dispersed without inducing significant viscous drag; allowing the flow characteristics to remain favorable [29]. Although the specific heat capacity of the nanofluid decreases by 29% due to the lower Cp of CuO, this drawback is mitigated by a 16.8% increase in thermal conductivity, which enhances the medium's ability to conduct heat more effectively. The trade-off between decreased specific heat and increased thermal conductivity is a well-documented phenomenon across various nanoparticle types and base fluids, including water, ethylene glycol, and molten salts, and is influenced by factors such as nanoparticle concentration, size, and dispersion quality [30]. The Reynolds number remains nearly unchanged (~0.35% increase), ensuring that the flow regime and velocity profile are preserved. Meanwhile, the Prandtl number drops by 39.4%, reflecting

enhanced thermal diffusivity relative to momentum diffusion; favorable for maintaining sharp thermal gradients and thinner thermoclines [31]. The combined effect results in a modest 2.5% improvement in the convective heat transfer coefficient. Most notably, the pressure drop per unit length reduces by 57.7%, indicating significantly lower flow resistance; likely due to improved thermal uniformity and reduced stratified flow zones [32]. Overall, the $CuO–N_2$ nanofluid formulation provides enhanced thermal transport and reduced hydraulic penalty, establishing it as a promising candidate for high-efficiency thermocline TES in CSP applications.

6. Conclusions

This study presents a comprehensive investigation of a packed-bed thermocline thermal energy storage (TES) system employing nitrogen as the heat transfer fluid, with a forward-looking extension toward $CuO–N_2$ nanofluid enhancement. A full-scale experimental setup was developed and operated to evaluate thermocline formation, axial temperature profiles, and pressure drops during high-temperature nitrogen charging cycles. Temperature data obtained from 16 thermocouples were used to validate a three-dimensional CFD model developed in ANSYS Fluent. The model accurately reproduced the downward thermal front propagation, stratification quality, and transient thermal behavior observed experimentally, achieving a mean absolute temperature error of below 3% and a pressure drop prediction within 10% of measured values.

The model incorporated Ergun-based porous media formulation and temperature-dependent nitrogen properties, with additional zones for support structures and filters. Detailed flow visualizations and pressure contour analyses confirmed uniform velocity distribution and thermally stable operation within the packed bed. These results confirm the CFD framework's robustness and accuracy, laying a reliable foundation for advanced parametric studies.

To address the thermal limitations of gas-phase HTFs, a nanofluid model based on CuO nanoparticles suspended in nitrogen was formulated. Using established correlations, the study quantified key thermophysical modifications at $\phi = 0.05\%$, including a +16.8% enhancement in thermal conductivity, a +2.5% gain in convective heat transfer coefficient, and a remarkable ~57.7% reduction in pressure drop per unit length. Despite a reduction in specific heat, the effective heat transfer potential improved due to stronger thermal gradients and minimal changes in viscosity.

Building on this foundation, the paper outlines a future CFD simulation campaign involving multiple nanoparticle volume fractions and proposes experimental modifications to enable real-time nanofluid testing. A dedicated nanoparticle injection system, updated flow circuits, and an inverter-controlled compressor have been integrated into the existing rig, enabling precise control and characterization of nanofluid dynamics under CSP-relevant conditions.

In conclusion, this work delivers a fully validated, high-resolution CFD–experimental benchmark of a gas-based thermocline TES system and proposes a detailed path for nanofluid integration. The combined framework of empirical validation, advanced modeling, and future experimental readiness offers valuable guidance for the development of compact, high-efficiency thermal energy storage units tailored to next-generation CSP technologies.

Nomenclature:

Abbreviations	
CFD	Computational Fluid Dynamis
CSP	Concentrated Solar Power

HTF	Heat Transfer Fluid
TES	Thermal Energy Storage
Dimensionless Numbers	
Pr	Prandtl number
Re	Reynolds number
Symbols	
d_p	Particle Diameter (m)
ε	Porosity
Φ	Volume concentration (%)
L	Length (m)
ρ	Density (kg/m^3)
u	Velocity (m/s)
μ	Viscosity (Pa·s)
h	Convective heat transfer coefficient (W/m^2·K)
k	Thermal conductivity (W/m·K)
ΔP	Pressure Drop
Cp	Specific capacity (J/kg.K)
Subscripts	
bf	Base fluid
nf	Nanofluid
np	Nanoparticle

Acknowledgement

We acknowledge financial support under the National Recovery and Resilience Plan (NRRP), Mission 4, Component 2, Investment 1.1, Call for tender No. 1409 published on 14.9.2022 by the Italian Ministry of University and Research (MUR), funded by the European Union – NextGenerationEU– Project Title Gases with nanoparticles as working fluid for CSP technologies (nanoCSP)– CUP F53D23009830001- Grant Assignment Decree No. 961 adopted on 30/06/2023 by the Italian Ministry of Ministry of University and Research (MUR).

References

[1] Răboacă M, Badea G, Enache A, Filote C, Răsoi G, Rață M, Lavric A, Felseghi R. Concentrating solar power technologies. *Energies*. 2019;12(6):1048. https://doi.org/10.3390/en12061048

[2] Cascetta M, Petrollese M, Oyekale J, Cau G. Thermocline vs. two-tank direct thermal storage system for concentrating solar power plants: A comparative techno-economic assessment. *Int J Energy Res*. 2021;45(12):17721–37. https://doi.org/10.1002/er.7005

[3] Achkari O, Fadar A. Latest developments on TES and CSP technologies – energy and environmental issues, applications and research trends. *Appl Therm Eng*. 2020;167:114806. https://doi.org/10.1016/j.applthermaleng.2019.114806

[4] Maia C, Neumann L, De Andrade Oliveira G, Alves Í, Walczak M, Brito P. A comprehensive review of solar tower CSP systems using TES and molten salts. *Int J Ambient Energy*. 2023;44:1733–47. https://doi.org/10.1080/01430750.2023.2185814

[5] Yılmaz İ, Mwesigye A, Kılıç F. Prioritization of heat transfer fluids in parabolic trough solar systems using CFD-assisted AHP-VIKOR approach. *Renew Energy*. 2023;213:1194–210. https://doi.org/10.1016/j.renene.2023.04.048

[6] Feng P, Zhao B, Wang R. Thermophysical heat storage for cooling, heating, and power generation: A review. *Appl Therm Eng*. 2020;166:114728. https://doi.org/10.1016/j.applthermaleng.2019.114728

[7] Zhang Y, Yao E, Zhang X, Yang K. Thermodynamic analysis of a novel compressed carbon dioxide energy storage system with low-temperature thermal storage. *Int J Energy Res*. 2020;44:6531–54. https://doi.org/10.1002/er.5387

[8] Mohamed Shameer P, Melesse TY, Orrù PF, Braggio M, Petrollese M. Next-generation CSP: The synergy of nanofluids and Industry 4.0 for sustainable solar energy management. *Energies*. 2025;18(8):2083. https://doi.org/10.3390/en18082083
[9] Mohamed Shameer P, Cascetta M, Migliari L, Petrollese M. Nanofluids in thermal energy storage systems: A comprehensive review. *Energies*. 2025;18(3):707. https://doi.org/10.3390/en18030707
[10] Han D, Lougou B, Shuai Y, Wang W, Jiang B, Shagdar E. Study of thermophysical properties of chloride salts doped with CuO nanoparticles for solar thermal energy storage. *Sol Energy Mater Sol Cells*. 2022;231:111432. https://doi.org/10.1016/j.solmat.2021.111432
[11] Aljaerani H, Samykano M, Pandey A, Kadirgama K, George M, Saidur R. Thermophysical properties enhancement and characterization of CuO nanoparticles enhanced HITEC molten salt for concentrated solar power applications. *Int Commun Heat Mass Transf*. 2022;137:105898. https://doi.org/10.1016/j.icheatmasstransfer.2022.105898
[12] Liu B, Liang W, Luo Z, Sarvar S, Fereidooni L, Kasaeian A. Performance improving of concentrated solar power systems with nanofluids: A review based on molecular dynamics. *J Mol Liq*. 2024;393:126052. https://doi.org/10.1016/j.molliq.2024.126052
[13] Graciano-Uribe J, Pujol T, Puig–Bargués J, Duran–Ros M, Arbat G, De Cartagena F. Assessment of different pressure drop-flow rate equations in a pressurized porous media filter for irrigation systems. *Water*. 2021;13(16):2179. https://doi.org/10.3390/w13162179
[14] King S, Nguyen T, Hassan Y. A pressure drop and particle image velocimetry investigation into depressurized loss-of-coolant accident parameters applied to packed beds with an aspect ratio of D/dp = 4.4. *Nucl Technol*. 2023;210:1245–57. https://doi.org/10.1080/00295450.2023.2259699
[15] Lopez M, Hocine A, Kone T, Dupont T, Panneton R. Inertial effects on single-perforation plates resistivity at high flow rates: Computational fluid dynamics and experimental studies. *J Acoust Soc Am*. 2025;157(2):1512–22. https://doi.org/10.1121/10.0035642
[16] Otaru A, Muhammad M, Samuel M, Olugbenga A, Gana M, Corfield M. Pressure drop in high-density porous metals via tomography datasets. *Metals Mater Int*. 2019;27:603–9. https://doi.org/10.1007/s12540-019-00431-y
[17] Lu X, Zhao Y, Dennis D. Fluid flow characterisation in randomly packed microscale porous beds with different sphere sizes using micro-particle image velocimetry. *Exp Therm Fluid Sci*. 2020;118:110136. https://doi.org/10.1016/j.expthermflusci.2020.110136
[18] Sekine M, Tsukamoto N, Masuhara Y, Furuya M. Experimental study on thermal stratification in water pool with vertical heat source. *Ann Nucl Energy*. 2024;195:110681. https://doi.org/10.1016/j.anucene.2024.110681
[19] Liu M, Zhang Y, Shi K, Zhu G, Wu Z, Liu M, Zhang Y. Thermal stratification dynamics in a large and deep subtropical reservoir revealed by high-frequency buoy data. *Sci Total Environ*. 2019;651(Pt 1):614–24. https://doi.org/10.1016/j.scitotenv.2018.09.215
[20] Lai Z, Hou C, Chen J, Guo X, Han G, Zhang K, Ding L, Lv H. Experimental study on energy storage characteristics of packed bed using different solid materials. *J Energy Storage*. 2024;82:113701. https://doi.org/10.1016/j.est.2024.113701
[21] Pacheco J, Showalter S, Kolb W. Development of a molten-salt thermocline thermal storage system for parabolic trough plants. *J Sol Energy Eng*. 2002;124:153–9. https://doi.org/10.1115/1.1464123
[22] Thomas B, Van Schalkwyk P, Engelbrecht J, Haase P, Maier A, Widmann C, Booysen M. Thermodynamic analysis of stratification in thermal energy storages implemented in cogeneration systems. *Appl Therm Eng*. 2023;226:121015. https://doi.org/10.1016/j.applthermaleng.2023.121015
[23] Sifnaios I, Jensen A, Furbo S, Fan J. Performance comparison of two water pit thermal energy storage (PTES) systems using energy, exergy, and stratification indicators. *J Energy Storage*. 2022;55:104947. https://doi.org/10.1016/j.est.2022.104947
[24] Bouziane H, Benhamou B. Assessment of the impact of thermal energy storage operation strategy on parabolic trough solar power plant performance. *Renew Energy*. 2023;202:12–23. https://doi.org/10.1016/j.renene.2022.11.119
[25] Mansour MA, Siddiqa S, Gorla RSR, Rashad AM. Effects of heat source and sink on entropy generation and MHD natural convection of Al_2O_3–Cu/water hybrid nanofluid filled with square porous cavity. *Therm Sci Eng Prog*. 2018;6:57–71. https://doi.org/10.1016/j.tsep.2017.10.014
[26] Bellos E, Tzivanidis C. Thermal analysis of parabolic trough collector operating with mono and hybrid nanofluids. *Sustain Energy Technol Assess*. 2018;26:105–15. https://doi.org/10.1016/j.seta.2017.10.005
[27] Pak BC, Cho YI. Hydrodynamic and heat transfer study of dispersed fluids with submicron metallic oxide particles. *Exp Heat Transf*. 1998;11:151–70. https://doi.org/10.1080/08916159808946559
[28] Ali B, Qayoum A, Saleem S, Mir F. Experimental investigation of nanofluids for heat pipes used in solar photovoltaic panels. *J Therm Eng*. 2023;9(3):342–52. https://doi.org/10.18186/thermal.1285179

[29] Asadi A, Alarifi I, Foong L. An experimental study on characterization, stability and dynamic viscosity of CuO–TiO_2/water hybrid nanofluid. *J Mol Liq*. 2020;310:112987. https://doi.org/10.1016/j.molliq.2020.112987
[30] Mirahmad A, Kumar R, Doldán B, Ríos C, Díez-Sierra J. Beyond thermal conductivity: A review of nanofluids for enhanced energy storage and heat transfer. *Nanomaterials*. 2025;15(4):302. https://doi.org/10.3390/nano15040302
[31] Rodríguez I, Campo A. Numerical investigation of forced convection heat transfer from a sphere at low Prandtl numbers. *Int J Therm Sci*. 2023;186:107970. https://doi.org/10.1016/j.ijthermalsci.2022.107970
[32] Daadoua M, Mathew B, Alnaimat F. Experimental investigation of pressure drop and heat transfer in minichannel with smooth and pin fin surfaces. *Int J Thermofluids*. 2024;19:100542. https://doi.org/10.1016/j.ijft.2023.100542